

# Journal of Materials Chemistry A

Materials for energy and sustainability

Accepted Manuscript

This article can be cited before page numbers have been issued, to do this please use: X. Dao, J. Guo, X. Zhang, S. Wang, X. Cheng and W. Sun, *J. Mater. Chem. A*, 2020, DOI: 10.1039/D0TA10278D.



This is an Accepted Manuscript, which has been through the Royal Society of Chemistry peer review process and has been accepted for publication.

Accepted Manuscripts are published online shortly after acceptance, before technical editing, formatting and proof reading. Using this free service, authors can make their results available to the community, in citable form, before we publish the edited article. We will replace this Accepted Manuscript with the edited and formatted Advance Article as soon as it is available.

You can find more information about Accepted Manuscripts in the [Information for Authors](#).

Please note that technical editing may introduce minor changes to the text and/or graphics, which may alter content. The journal's standard [Terms & Conditions](#) and the [Ethical guidelines](#) still apply. In no event shall the Royal Society of Chemistry be held responsible for any errors or omissions in this Accepted Manuscript or any consequences arising from the use of any information it contains.

## ARTICLE

**Structure-dependent iron-based metal-organic frameworks for selectively CO<sub>2</sub>-to-CH<sub>4</sub> photocatalytic reduction†**Xiao-Yao Dao,<sup>‡</sup> Jin-Han Guo,<sup>‡</sup> Xiao-Yu Zhang, Shi-Qing Wang, Xiao-Mei Cheng and Wei-Yin Sun\*Received 00th January 20xx,  
Accepted 00th January 20xx

DOI: 10.1039/x0xx00000x

Visible-light driven reduction of carbon dioxide (CO<sub>2</sub>) to methane (CH<sub>4</sub>) is a challenge in the photocatalytic reaction system. Herein, two Fe-based metal-organic frameworks (MOFs) MIL-100(Fe) and MIL-101(Fe) with single-trimetallic clusters but distinct organic ligands were employed to explore the structure-dependent CO<sub>2</sub> conversion performance. Compared with MIL-101(Fe), MIL-100(Fe) exhibits superior catalytic activity and selectivity for CH<sub>4</sub> generation under visible-light irradiation via a solvent-free route. This is the first report that MIL-100(Fe) finishes photoreduction of CO<sub>2</sub> into CH<sub>4</sub>. Importantly, the plausible conversion pathways of the reaction were given by density functional theory (DFT) calculations. This work furnishes new direction for constructing MOFs to achieve CO<sub>2</sub>-to-CH<sub>4</sub> conversion.

**Introduction**

Photoreduction of CO<sub>2</sub> to high value-added products utilizing sustainable solar energy as the reaction impetus is a pursuable way to accomplish CO<sub>2</sub> recycling, alleviating greenhouse effect and energy crisis.<sup>1-3</sup> However, CO<sub>2</sub> has high C=O bond energy, CO<sub>2</sub> photoreduction has to overcome such high energy barriers to dissociate the C=O bond.<sup>4</sup> Generally, the photon-assisted CO<sub>2</sub> reduction process can produce a series of products from two-electron to eight-electron products.<sup>5-6</sup> The eight-electron product of CH<sub>4</sub> is the desirable hydrocarbon fuels in the photocatalytic system, but at the same time, is harder to achieve than the two-electron products of formic acid (HCOOH) and carbon oxide (CO).<sup>7</sup>

Since Lin and co-workers reported that CO<sub>2</sub> photoreduction was realized by incorporating Re(CO)<sub>3</sub>(5,5'-cbpy)Cl into the framework of UiO-67.<sup>8</sup> Metal-organic frameworks (MOFs), consisting of metal nodes and flourishing types of organic linkers, are considered as a kind of promising photocatalysts for performance regulation.<sup>9-17</sup> Furthermore, MOFs containing high-density metal nodes provide abundant coordinatively unsaturated metal sites (CUS) that have attracted mounting attention for potential redox activity.<sup>18,19</sup> In addition, the flourishing types of multidentate organic ligands can be rationally designed and/or modified to regulate the catalytic performance.<sup>20-22</sup> To date, the majority of studies on MOF materials has been reported with primary focus on HCOOH/CO production.<sup>23-29</sup> Only several of pristine MOFs present the selectivity for CH<sub>4</sub> generation, such as MOF-525, Zn/PMOF,

NENU-605/606, NNU-13/14 and PCN-601.<sup>30-34</sup> Undeniable, it is a challenge to develop the diversity of photocatalysts, which is remarkable and attractively promising for facilitating efficiency and selectivity of CO<sub>2</sub> conversion into CH<sub>4</sub>.

Different series of MOFs with CUS and trimetallic nodes emerge in the MOFs such as MIL-88B(Fe), MIL-100(Fe, Cr), MIL-101(Fe, Cr), PCN-250 (Fe<sub>3</sub>, Fe<sub>2</sub>Mn, Fe<sub>2</sub>Co, and Fe<sub>2</sub>Ni), NNU-31 (Fe<sub>2</sub>Co, Fe<sub>2</sub>Ni, Fe<sub>2</sub>Zn).<sup>35-42</sup> The trimetallic clusters with CUS make these MOFs as a charming platform for redox catalysis. For instance, trimetallic cluster-based PCN-250 (Fe<sub>3</sub>, Fe<sub>2</sub>Co, and Fe<sub>2</sub>Ni) exhibit superior reactivity towards CO<sub>2</sub>-to-CO transformation.<sup>41</sup> The mixed-metal-containing MOFs of NNU-31 (Fe<sub>2</sub>Co, Fe<sub>2</sub>Ni, Fe<sub>2</sub>Zn) display excellent photocatalytic CO<sub>2</sub> reduction performance to achieve high efficiency for CO<sub>2</sub>-to-HCOOH conversion.<sup>42</sup> Additionally, single-metal-based NH<sub>2</sub>-MIL-101(Fe) and NH<sub>2</sub>-MIL-88B(Fe) with amino-functionalized organic linkers display superior selectivity for conversion of CO<sub>2</sub> to HCOOH or CO.<sup>25,29</sup> MOFs with mixed-trimetallic clusters have been synthesized and thoroughly studied for catalytic reactions, further reveal the relationship of the metal node composition on the catalytic performance.<sup>42-44</sup> However, few reports reveal the relationship of the distinct ligands with single-trimetallic clusters on the photocatalytic performance,<sup>20,45-48</sup> especially for CO<sub>2</sub> photoreduction.

Herein, MOFs of MIL-100(Fe) and MIL-101(Fe) with single-trimetallic clusters but distinct ligands were employed for studies on photocatalytic performance. These characters make MOFs as the desired platform to explore the impact of ligand on the catalytic reactivity and to uncover structure-performance correlation. The results confirm the superior reactivity of MIL-100(Fe) towards CO<sub>2</sub> photoreduction into CH<sub>4</sub>. The CH<sub>4</sub> production yield of MIL-100(Fe) exceeds at least 16.5 times of MIL-101(Fe). This is the first report that MIL-100(Fe) finishes photoreduction of CO<sub>2</sub> into CH<sub>4</sub>. Furthermore, the plausible reduction pathways of the optimal photocatalyst were confirmed by density functional theory (DFT) calculations.

Coordination Chemistry Institute, State Key Laboratory of Coordination Chemistry, School of Chemistry and Chemical Engineering, Nanjing National Laboratory of Microstructures, Collaborative Innovation Center of Advanced Microstructures, Nanjing University, Nanjing 210023, China. Email address: sunwy@nju.edu.cn; Tel: +86 25 89683485

†Electronic Supplementary Information (ESI) available: SEM, CO<sub>2</sub> uptake, M-S plots <sup>1</sup>H NMR, GC-MS, and other tables and figures. See DOI: 10.1039/x0xx00000x

‡ These authors contributed equally to this work.

## Experimental

### Density functional theory (DFT) calculations

All spin-polarized DFT computations were performed by using Vienna ab-initio simulation package (VASP) based on projector augmented wave (PAW) method.<sup>49-51</sup> Electron-ion interactions were described using standard PAW potentials with valence configurations of  $2s^2 2p^6 3s^2 3d^6$  for Fe,  $2s^2 2p^2$  for C,  $2s^2 2p^4$  for O, and  $1s^1$  for H.<sup>52,53</sup> A plane-wave basis set was employed to expand the smooth part of wave functions with a cut-off kinetic energy of 480 eV. For electron-electron exchange and correlation interactions, the functional parameterized by Perdew-Burke-Ernzerhof (PBE),<sup>54</sup> a form of general gradient approximation (GGA), was used throughout. Due to insufficient consideration of the on-site Columbic repulsion, DFT might fail to describe the electronic structure of the MIL-100(Fe) and MIL-101(Fe). To overcome this shortcoming, the GGA+U approach was used with  $U - J = 6.0$  eV for Fe atoms.<sup>55</sup> Since the unit cells of MIL-100(Fe) and MIL-101(Fe) contain more than 10,000 atoms, the calculation on such big systems was beyond the computational power of current supercomputer. Considering that the building block of MIL-100(Fe) and MIL-101(Fe) is a super tetrahedral cell, which includes  $\text{Fe}_3\text{O}(\text{COO})_6$  trimers connected by BTC or BDC ligands, the active reaction center for MIL-100(Fe) and MIL-101(Fe) is 5-coordinated metal ions in trimers for adsorption of  $\text{CO}_2$ . A finite-size cluster model  $\text{Fe}_3\text{O}$  trimer, which is cut from the periodic structure, was adopted to approximate the structure. The Brillouin-zone integrations were performed using the Gamma-point only grid. When the geometries were optimized, all atoms were allowed to relax. And the atomic structures were optimized until the residual forces were below  $0.02$  eV/Å. Gas-phase molecules were treated using the ideal gas approximation, whereas adsorbates were treated using a harmonic approximation. The DFT-calculated energy for  $\text{CO}_2$  was corrected by  $+0.45$  eV,<sup>56</sup> a usual adjustment to correct the overestimation by DFT.  $\text{H}_2\text{O}$  was calculated under  $0.035$  atm. The relative free energies were calculated based on the computational hydrogen electrode (CHE) model.<sup>57</sup>

The Gibbs free energy ( $\Delta G$ ) of each reaction step is defined as the difference between the free energy of the reaction initiation and termination states, and the general formula is described as

$$\Delta G = \Delta E_{\text{DFT}} + \Delta E_{\text{ZPE}} - T\Delta S$$

where  $E_{\text{DFT}}$  is the electronic energy obtained from DFT calculations of the catalysts,  $\Delta E_{\text{ZPE}}$  is the change of zero-point energy,  $T\Delta S$  is the entropy contribution. Zero-point energies and entropies of photocatalytic  $\text{CO}_2$  reduction of intermediates were computed from the vibrational frequencies.

Therefore, free energy changes relative to an initial state of gaseous  $\text{CO}_2$  free above an empty surface can be displayed by:

$$\Delta G[*\text{COOH}] = G[*\text{COOH}] + 7 \times G[\text{H}^+ + \text{e}^-] - (G[*] + G[\text{CO}_2] + 8 \times G[\text{H}^+ + \text{e}^-])$$

$$\Delta G[*\text{CO}] = G[*\text{CO}] + G[\text{H}_2\text{O}] + 7 \times G[\text{H}^+ + \text{e}^-] - (G[*] + G[\text{CO}_2] + 8 \times G[\text{H}^+ + \text{e}^-])$$

$$\Delta G[*\text{CHO}] = G[*\text{CHO}] + G[\text{H}_2\text{O}] + 5 \times G[\text{H}^+ + \text{e}^-] - (G[*] + G[\text{CO}_2] + 8 \times G[\text{H}^+ + \text{e}^-])$$

$$\Delta G[*\text{CO}] = G[*\text{CO}] + G[\text{H}_2\text{O}] + 7 \times G[\text{H}^+ + \text{e}^-] - (G[*] + G[\text{CO}_2] + 8 \times G[\text{H}^+ + \text{e}^-])$$

$$\Delta G[\text{CH}_2\text{O}] = G[*] + G[\text{CH}_2\text{O}] + G[\text{H}_2\text{O}] + 4 \times G[\text{H}^+ + \text{e}^-] - (G[*] + G[\text{CO}_2] + 8 \times G[\text{H}^+ + \text{e}^-])$$

$$\Delta G[*\text{OCH}_3] = G[\text{CH}_3\text{O}*] + G[\text{H}_2\text{O}] + 3 \times G[\text{H}^+ + \text{e}^-] - (G[*] + G[\text{CO}_2] + 8 \times G[\text{H}^+ + \text{e}^-])$$

$$\Delta G[\text{CH}_3\text{OH}*] = G[\text{CH}_3\text{OH}*] + G[\text{H}_2\text{O}] + 2 \times G[\text{H}^+ + \text{e}^-] - (G[*] + G[\text{CO}_2] + 8 \times G[\text{H}^+ + \text{e}^-])$$

$$\Delta G[*\text{OH}] = G[*\text{OH}] + G[\text{H}_2\text{O}] + G[\text{CH}_4] + G[\text{H}^+ + \text{e}^-] - (G[*] + G[\text{CO}_2] + 8 \times G[\text{H}^+ + \text{e}^-])$$

$$\Delta G[\text{CH}_4 + 2\text{H}_2\text{O}] = G[*] + G[\text{CH}_4] + 2 \times G[\text{H}_2\text{O}] - (G[*] + G[\text{CO}_2] + 8 \times G[\text{H}^+ + \text{e}^-])$$

### Electrochemical measurements

Photocurrent measurements were performed on a CHI 730E electrochemical work station (Chenhua Instrument, Shanghai, China) in a standard three-electrode system with photocatalyst-coated ITO as working electrode, Pt plate as counter electrode, and Ag/AgCl as reference electrode.  $\text{CH}_3\text{CN}$  solution of  $0.1$  M ( $n\text{-Bu}$ )<sub>4</sub>N(PF<sub>6</sub>) was used as electrolyte. The as-synthesized sample ( $5$  mg) was added into  $20$   $\mu\text{L}$  Nafion and  $2.0$  mL ethanol solution, and the working electrode was prepared by dropping the suspension ( $200$   $\mu\text{L}$ ) onto the surface of an ITO plate. The working electrode was dried at room temperature, and the photo-responsive signals of the samples were measured under chopped light at  $0.5$  V.

The electrochemical impedance spectroscopy (EIS) was performed on the Zahner electrochemical workstation in a standard three-electrode system with the photocatalyst-coated carbon paper as working electrode, Pt plate as counter electrode and Ag/AgCl as reference electrode. A  $0.2$  M  $\text{Na}_2\text{SO}_4$  solution was used as electrolyte. The working electrode was prepared by dropping the ink ( $200$   $\mu\text{L}$ ) onto the surface of the carbon paper. The working electrode was dried at room temperature, and then EIS measurements were performed with a bias potential of  $-0.5$  V in the dark with a frequency range from  $10^{-2}$  to  $10^5$  Hz under nitrogen atmosphere. The Mott-Schottky test was performed on the Zahner electrochemical workstation in a standard three-electrode system with the photocatalyst-coated glassy carbon as working electrode, Pt plate as counter electrode and Ag/AgCl as reference electrode. A  $0.2$  M  $\text{Na}_2\text{SO}_4$  solution was used as electrolyte. The working electrode was prepared by dropping the ink ( $50$   $\mu\text{L}$ ) onto the surface of glassy carbon and dried at room temperature. The measurements were carried out with different frequencies of  $1000$ ,  $2000$  and  $3000$  Hz.

### Photocatalytic reduction of $\text{CO}_2$ experiments

The photocatalytic reduction of  $\text{CO}_2$  experiments were carried out in a batch-type reaction system (CEL-SPH2N-D9, CeAulight, China) equipped with a homemade gas-solid reactor (Fig. S1†). The photocatalyst ( $2$  mg) was uniformly dispersed into a circular glass-fibre membrane ( $0.22$   $\mu\text{m}$  pore diameter) with an illuminated area of about  $2.8$   $\text{cm}^2$ . The membrane activated in vacuum at  $150$   $^\circ\text{C}$  for  $12$  h. Subsequently, the membrane was installed in the reactor with the distance from the light source to the sample was  $11$  cm and TEOA ( $2$  mL) was added into the reactor. The reaction system was completely vacuumed and pumped with  $\text{CO}_2$  gas. A  $300$  W xenon arc lamp (Sirius-300P,

Zolix Instruments Co., Ltd., China) with a 400–780 nm filter was used as the light source. The optical power density remained at 400 mW cm<sup>-2</sup> measured by an optical power meter (CEL-NP2000-2, CeAulight, China). The gas products were analyzed

by gas chromatography (GC-9860, Luchuang Instrument, China). The <sup>13</sup>CO<sub>2</sub> isotopic labelling was determined by using a gas chromatography-mass spectrometer (Trace GC Ultra, ThermoFisher Scientific).

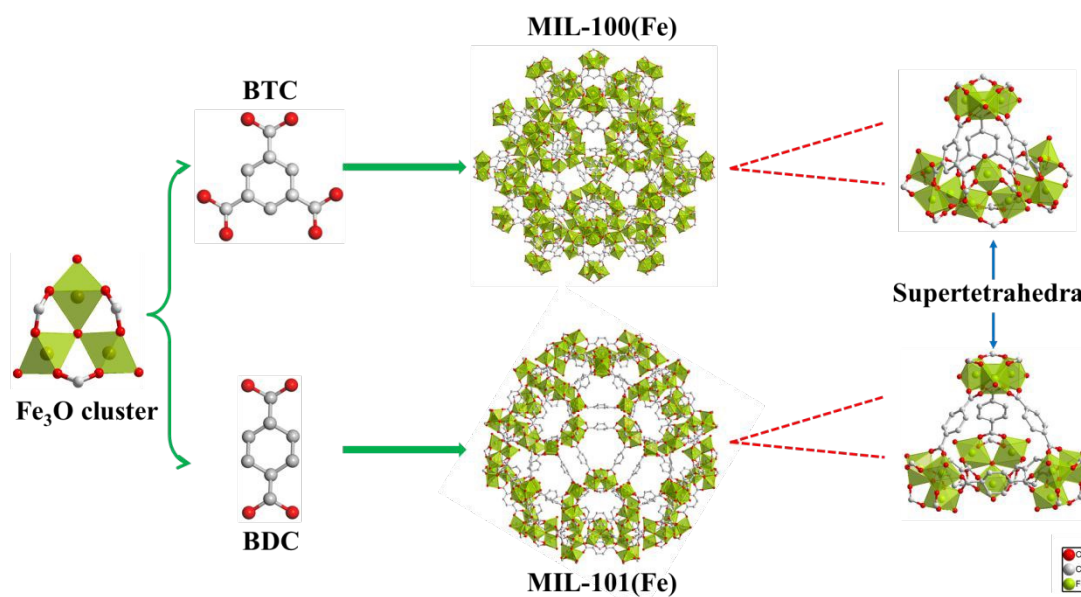


Fig. 1 Schematic illustration of MIL-100(Fe) and MIL-101(Fe) with Fe<sub>3</sub>O clusters and BTC and BDC ligands. Color code: O, red; C, gray; Fe, green.

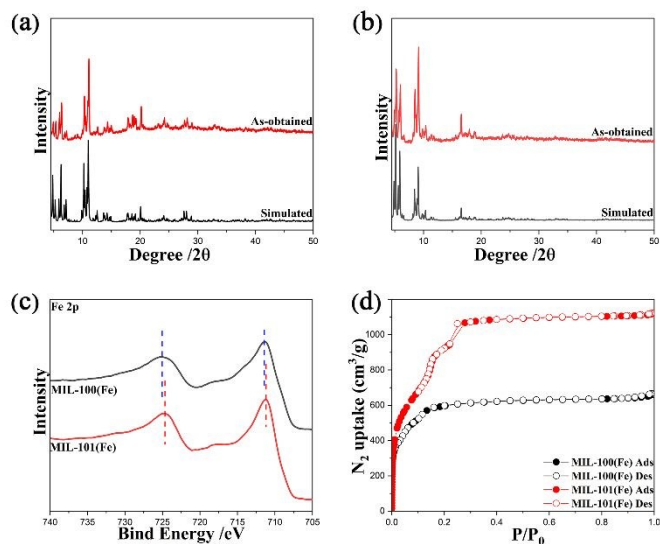


Fig. 2 XRD patterns of MIL-100(Fe) (a) and MIL-101(Fe) (b). XPS spectra of MIL-100(Fe) and MIL-101(Fe): Fe 2p spectra (c) and N<sub>2</sub> adsorption-desorption isotherms of MIL-100(Fe) and MIL-101(Fe) (d).

## Results and discussion

MOFs MIL-100(Fe) and MIL-101(Fe) were synthesized and characterized in a conventional way (Fig. 1). The morphologies of the as-prepared samples display monodispersed nanocrystals and present typical octahedral-shaped

morphology (Fig. S2<sup>†</sup>). The as-obtained samples reveal well-distinguished diffraction peaks that matched well with the simulated ones, demonstrating the framework structures were achieved successfully (Fig. 2a and 2b).<sup>36,38</sup> X-ray photoelectron spectroscopy (XPS) was further employed to determine the composition and chemical environment of MIL-100(Fe) and MIL-101(Fe). From the survey scanning spectrum (Fig. S3<sup>†</sup>), it can be found the existence of Fe, C, and O in both samples. The high-resolution spectra of Fe 2p of MIL-100(Fe) and MIL-101(Fe) are exhibited in Fig. 2c. Compared with MIL-100(Fe), the peaks of MIL-101(Fe) display tiny negative shifts, indicating the electron-density on Fe<sub>3</sub>O clusters is enhanced.<sup>45</sup> This result further confirms that the bridging-ligands influence the local electron-density of the metal nodes. The porosity of MIL-100(Fe) and MIL-101(Fe) were determined by N<sub>2</sub> adsorption-desorption isotherms (Fig. 2d) with BET surface areas of 2147.6 and 3663.5 m<sup>2</sup>/g, respectively. Compared with MIL-101(Fe), MIL-100(Fe) displays higher absorption capacity (97.2 cm<sup>3</sup>/g at 273 K) and larger adsorption enthalpy (39.4 kJ/mol) for CO<sub>2</sub> (Figs. S4, S5 and S6<sup>†</sup>), indicating the relatively more robust CO<sub>2</sub>-framework interactions in MIL-100(Fe). The results imply that MIL-100(Fe) has kinetically advantage for CO<sub>2</sub> transformation.<sup>58</sup>

UV-vis diffuse reflectance spectroscopy (UV-DRS) was employed to evaluate the optical-response and the results display that both samples have optical absorption covering the UV-visible region owing to the presence of μ-O-Fe clusters (Fig. 3a).<sup>59</sup> The bandgap of MIL-100(Fe) and MIL-101(Fe) are identified to be about 2.65 and 2.08 eV, respectively (Fig. S7<sup>†</sup>).

Mott-Schottky (MS) measurements were performed to determine the conduct band (LUMO) of MIL-100(Fe) and MIL-101(Fe). The positive slopes imply typical n-type semiconductor-like character. The flat-band potentials of MIL-100(Fe) and MIL-101(Fe) are determined to be -0.98 and -1.04 V vs. normalized hydrogen electrode (NHE), respectively (Fig. S8†). The potentials of these samples are more negative than the redox potential of CO<sub>2</sub> to CO (-0.53 V vs. NHE) as well as to CH<sub>4</sub> (-0.24 V vs. NHE), accordingly, these materials have capability for CO<sub>2</sub> photoreduction. Besides, to assess the separation efficiency of photo-excited charge carriers, photocurrent response was measured with the illumination of visible-light. As illustrated in Fig. 3b, MIL-100(Fe) possesses higher photocurrent than MIL-101(Fe), reflecting that MIL-100(Fe) has more efficient interface charge separation. Additionally, electrochemical impedance spectroscopy (EIS) for MIL-100(Fe) implies low resistance in the Nyquist plots (Fig. 3c), also indicating the fast interface charge transfer. Furthermore, the time-resolved photoluminescence (PL) decay spectra suggest that the average PL lifetimes of MIL-100(Fe) and MIL-101(Fe) are calculated to be 0.46 and 0.25 ns, respectively (Fig. 3d). The prolonged lifetime further proves that the free charges in MIL-100(Fe) may transfer for more extended until recombination. On account of the efficient charge separation and prolonged charge lifetime, MIL-100(Fe) can be considered as a desired photocatalyst for CO<sub>2</sub> reduction.

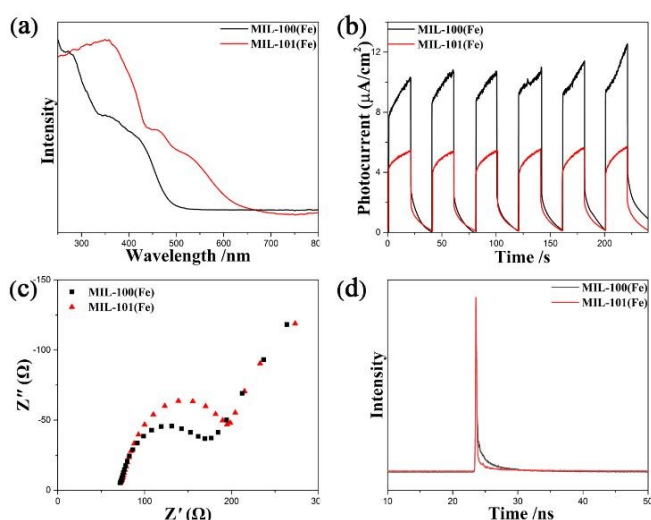


**Fig. 3** Diffuse reflectance UV/vis spectra (a), transient photocurrents (b), EIS Nyquist plots (c) and time-resolved fluorescence spectra (d) of MIL-100(Fe) (black-line) and MIL-101(Fe) (red-line).

Visible-light driven photoreduction of CO<sub>2</sub> was conducted via a solvent-free reaction route by utilizing triethanolamine (TEOA) as sacrificial agent. As displayed in Fig. 4, two samples exhibit distinct yields of transformation CO<sub>2</sub> to CO and CH<sub>4</sub> in five hours under the visible-light irradiation (Fig. S9† with calibration curves and Fig. S10†). In order to monitor the liquid products, <sup>1</sup>H NMR spectral measurements were conducted, and no liquid product was detected in the catalytic process (Fig. S11†), which may be due to the employment of solvent-free reaction system.<sup>26,29,31</sup> Additionally, no H<sub>2</sub>-production was detected by gas chromatography (GC) during the whole

catalytic process (Fig. S12†). Clearly, MIL-100(Fe) exhibits superior catalytic activity with CO and CH<sub>4</sub> generation. Importantly, the MIL-100(Fe) achieves high selectivity of about 98% for CH<sub>4</sub> formation (relative to the total number of reacted electrons) (Fig. S13†). Meanwhile, MIL-101(Fe) displays limited catalytic activity with CO and CH<sub>4</sub> production. Thus, MIL-100(Fe) possesses superior selectivity and activity for CO<sub>2</sub> conversion into CH<sub>4</sub>. In addition, solar-to-methane (CH<sub>4</sub>) conversion efficiency ( $\eta\%$ ) and apparent quantum efficiency (AQY%) over MIL-100(Fe) are 0.023% and 0.943%, respectively. It is noticeable that MIL-100(Fe) gives high AQY compared with the MIL-101(Fe) and reported heterogeneous photocatalysts (Table S1†). To further illustrate the photocatalytic activity, the turnover frequencies (TOF) of these catalysts were determined by the amount of metal active sites, and corresponding TOF values of these photocatalysts are displayed in Fig 4a.

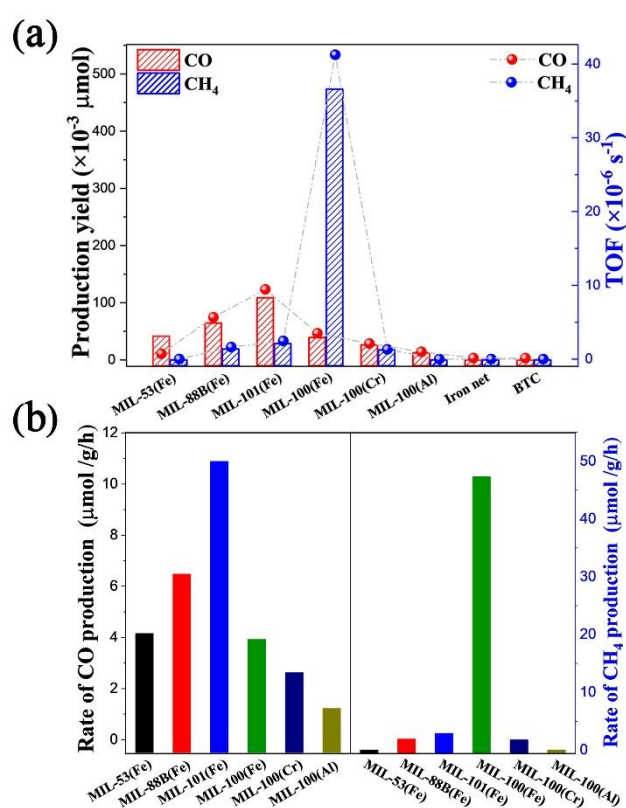


**Fig. 4** (a) Photocatalytic CO<sub>2</sub> into CO and CH<sub>4</sub> production and corresponding TOF values and (b) comparison of CO (left) and CH<sub>4</sub> (right) generation rate of varied photocatalysts.

In order to verify the carbon origins of the target products of CO and CH<sub>4</sub>, <sup>13</sup>C-labeled <sup>13</sup>CO<sub>2</sub> was applied for the photocatalytic test. The reaction products <sup>13</sup>CO and <sup>13</sup>CH<sub>4</sub> were confirmed by mass spectrometry (Fig. S14†), ensuring that both goal products resulted from CO<sub>2</sub> reduction. To further explore the photocatalytic activity of MIL-100(Fe), we compared the photocatalytic activity of MIL-100(Fe) with additional catalysts (Fig. 4a) such as MIL-100(Cr, Al), MIL-88B(Fe) and MIL-53(Fe). All samples exhibit weak photocatalytic activity. Additionally, the constituents of MIL-100(Fe), including iron net and BTC, give an insignificant photocatalytic effect (Fig. 4), thus indicating the importance of the MIL-100(Fe) skeleton for the photocatalytic

reaction. According to the previous work,<sup>29</sup> NH<sub>2</sub>-MIL-101(Fe) possesses a superior selectivity for conversion of CO<sub>2</sub> to CH<sub>4</sub>. More importantly, the order of CH<sub>4</sub>-yield is MIL-100(Fe) > MIL-101(Fe) > MIL-88B(Fe) > NH<sub>2</sub>-MIL-101(Fe). Meanwhile, the order of CO-yield is NH<sub>2</sub>-MIL-101(Fe) > MIL-101(Fe) > MIL-88B(Fe) > MIL-100(Fe) (Table S2<sup>†</sup>). These results demonstrate that the photocatalytic performance of Fe-based MOFs was improved by changing organic ligand with identical Fe-oxo clusters. In addition, the different performance of these photocatalysts may also be attributed to their unique framework structures. MIL-100(Fe) and MIL-101(Fe)/NH<sub>2</sub>-MIL-101(Fe) possess uniform Fe-oxo clusters and four μ<sub>3</sub>-O-bridged Fe<sub>3</sub>O clusters together constitute a tetrahedron as structural unit (Fig. S15<sup>†</sup>). For MIL-101(Fe) or NH<sub>2</sub>-MIL-101(Fe), terephthalate (BDC) or amino-substituted terephthalate (NH<sub>2</sub>-BDC) ligands as the edge of tetrahedron connect with Fe<sub>3</sub>O clusters, while MIL-100(Fe) with tricarboxylate (BTC) one as the facet of tetrahedron coordinates with the Fe<sub>3</sub>O clusters. Comparatively speaking, the structural unit of MIL-100(Fe) is more closely arranged than the one of MIL-101(Fe) or NH<sub>2</sub>-MIL-101(Fe) (Fig. S16<sup>†</sup>), in which closely packed tetrahedron structure is conducive to the migration of electrons. Furthermore, MIL-100(Fe) has greater Fe<sub>3</sub>O cluster density than MIL-101(Fe) within the same photocatalytic area (Fig. S17<sup>†</sup>), in which the CO<sub>2</sub> photoreduction occurs. As for MIL-88B(Fe), with the triangular bipyramidal arrangement of five Fe<sub>3</sub>O clusters (Fig. S18<sup>†</sup>), the structure unit is loosely arranged than the tetrahedron as the structural unit, and further results poor photocatalytic activity than MIL-100(Fe) and MIL-101(Fe). More significantly, the electrophilicity of coordinated organic ligands follows the order: NH<sub>2</sub>-BDC < BDC < BTC, and MIL-100(Fe) displays a more efficient inter-cluster delocalization.<sup>45,60</sup> Hence, the excellent photocatalytic activity of MIL-100(Fe) can be attributed to the closely arranged structural units, BTC with high electrophilicity and further reduced electron-density of the Fe<sub>3</sub>O clusters. Furthermore, a series of control tests were conducted in the vacuum or dark or without photocatalyst or TEOA. The target products were undetectable in these catalytic systems (Table S3<sup>†</sup>). Importantly, the photostability of MIL-100(Fe) was evaluated using recycling experiments. As shown in Fig. S19<sup>†</sup>, MIL-100(Fe) exhibits the long-term photocatalytic stability after multiple uninterrupted cycles. Corresponding SEM image, PXRD pattern and XPS spectra after the photocatalysis were shown in Figs. S20-S22<sup>†</sup>. The post-catalyst retained the octahedral morphology after multiple photocatalytic test, except that its surface became rough. These results demonstrate that the morphology, crystalline-structure and oxidation state of MIL-100(Fe) have no noticeable alteration, confirming the structural robustness.

DFT calculations were performed to get further insight into the CO<sub>2</sub>-to-CH<sub>4</sub> reaction process.<sup>4, 61-63</sup> The computations are assuming converted proton-electron transfer and evaluated at 0 V vs. RHE. The Gibbs free energy diagrams of the reaction pathways are illustrated in Fig 5, the formation of \*COOH on MIL-100(Fe) and MIL-101(Fe) are endothermic processes with energy barriers of 1.906 and 2.005 eV, respectively. And the formation of \*COOH is considered as the rate-determining step

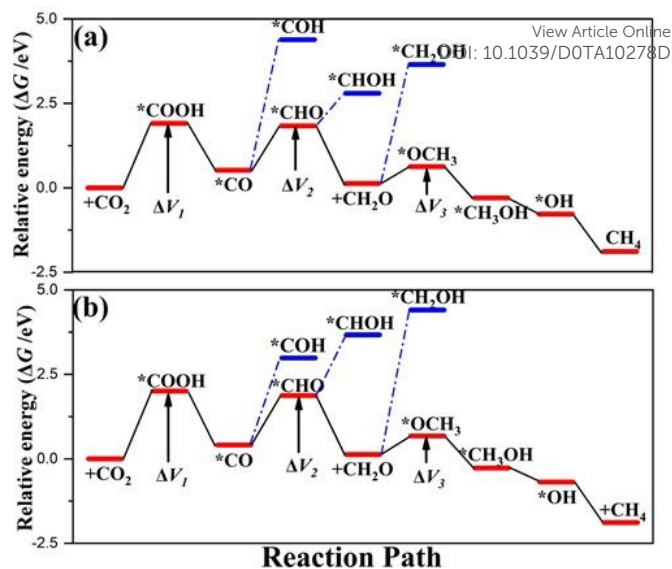


Fig. 5 DFT calculations. Free energy diagram of photocatalytic reduction CO<sub>2</sub>-to-CH<sub>4</sub> for MIL-100(Fe) (a) and MIL-101(Fe) (b). Optimal pathways to CH<sub>4</sub> and the three limited potential steps are shown by ΔV<sub>1</sub>, ΔV<sub>2</sub>, and ΔV<sub>3</sub>. The black line indicates a path with lower limited potential, and the blue line indicates a competitive path. \* The active surface sites for adsorption and reaction.

for both catalysts. The \*COOH intermediate can react with proton-electron and forming \*CO, which is connected with the Fe-O clusters. Subsequently, the protonation reaction of \*CO can produce two potential intermediates: \*CHO or \*COH. The relative potentials between \*CO and \*COH are too high to be realized. This fact indicates that the \*CHO intermediate is preponderant in this step. From Fig. 5, the reaction process of \*CHO to CH<sub>4</sub> are thermodynamically favorable, except that the reduction process of CH<sub>2</sub>O(g) to \*OCH<sub>3</sub> requires to meet energy demands. Therefore, the optimal reaction path for CO<sub>2</sub>-to-CH<sub>4</sub> on MIL-100(Fe) and MIL-101(Fe) follows CO<sub>2</sub> → \*COOH → \*CO → \*CHO → CH<sub>2</sub>O(g) → \*OCH<sub>3</sub> → \*CH<sub>3</sub>OH → \*OH → CH<sub>4</sub>(g). The stable structures corresponding to the optimal reaction path are displayed in Figs. S23 and S24<sup>†</sup>. Between the samples, the ΔV of the corresponding endothermic processes on MIL-100(Fe) is lower than that on MIL-101(Fe) (Table S4<sup>†</sup>), which demonstrated that the MIL-100(Fe) would be a more efficient photocatalyst for CO<sub>2</sub> reduction. Besides, the CO temperature-programmed desorption (TPD) measurement was employed to reveal the CO desorption process on the photocatalyst surface (Fig. S25<sup>†</sup>). The results suggest that the stronger interaction between CO and MIL-100(Fe) can more efficiently prevent CO to escape from the Fe-O clusters, which benefits for further hydrogenation of CO to generate CH<sub>4</sub>. This result is in agreement with the photocatalytic experiment, in which MIL-100(Fe) shows superior selectivity and reactivity for CO<sub>2</sub>-to-CH<sub>4</sub>. The choice of CO, HCHO and CH<sub>3</sub>OH feeds was based on the calculational results that all of them may constitute reactive intermediates of the catalytic process.<sup>33, 61, 64</sup> Therefore, taking the optimal catalyst of MIL-100(Fe), the photocatalytic experiment under CO, HCHO, and CH<sub>3</sub>OH were applied separately as feed reactants (Fig. S26<sup>†</sup>), the result proved that CO, HCHO, and CH<sub>3</sub>OH are the intermediates for CH<sub>4</sub> formation, which is in line with the DFT predictions.

On the basis of the above results, a possible reaction pathway of visible-light-driven CO<sub>2</sub> photoreduction over MIL-100(Fe) was proposed. Compared with MIL-101(Fe), MIL-100(Fe) not only possesses superior CO<sub>2</sub> adsorption capacity because there are more interaction sites on the surface, but also displays acceleration of electron transfer owing to the closely packed structure units. In addition, the flat-band potentials of MIL-100(Fe) and MIL-101(Fe) satisfy the thermodynamic demand for the CO<sub>2</sub> transformation into CH<sub>4</sub>. Upon visible-light irradiation, the photogenerated electrons migrate to the surface of the catalysts, where the adsorbed CO<sub>2</sub> captures electron to form \*COOH. Then, adsorbed CO<sub>ads</sub> may form after proton-electron coupled-reactions with \*COOH. The strong interaction between CO<sub>ads</sub> and MIL-100(Fe) can prevent CO to escape from the photocatalyst surface, confirmed by the fact that only a small amount of CO was detected in the products, which is favorable for further hydrogenation of CO<sub>ads</sub> to generate CH<sub>4</sub>. With the combined advantages, the CO<sub>ads</sub> on the surface of MIL-100(Fe) would be more efficiently converted into CH<sub>4</sub> than those on MIL-101(Fe). As a result, MIL-100(Fe) exhibits outstanding photocatalytic performance with remarkable selectivity toward CH<sub>4</sub>.

## Conclusions

In summary, the Fe-based MOF MIL-100(Fe) exhibits superior reactivity for CO<sub>2</sub> photoreduction compared with MIL-101(Fe). More importantly, MIL-100(Fe) achieves outstanding activity and high selectivity for CH<sub>4</sub> formation. Meanwhile, the ligand variations could influence the local electron-density of metal nodes, the structural unit of the frameworks, and further a high capacity density of Fe<sub>3</sub>O clusters with MIL-100(Fe) can accelerate the migration of photogenerated electron-hole to improve the efficiency of the catalytic reaction. Finally, the DFT calculations give the optimal reaction pathways from CO<sub>2</sub> to CH<sub>4</sub> catalyzed by MIL-100(Fe) and MIL-101(Fe), and further unveil the relationship between structure (bridging ligand and metal clusters) and performance (CO<sub>2</sub> photoreduction). Thus, this work will open windows to construct various high-activity photocatalysts by precisely modulating the composition of metal clusters and organic ligands.

## Conflicts of interest

There are no conflicts to declare.

## Acknowledgements

We gratefully acknowledge the National Basic Research Program of China (grant no. 2017YFA0303504) and the Fundamental Research Funds for the Central Universities (grant no. 14380232) for financial support of this work. This work was also supported by a Project Funded by the Priority Academic Program Development of Jiangsu Higher Education Institutions. We are grateful to the High Performance Computing Center of

Nanjing University for conducting the DFT calculation in this work on its Flex cluster system. DOI: 10.1039/D0TA10278D

## Notes and references

- S. C. Roy, O. K. Varghese, M. Paulose, C. A. Grimes, *ACS Nano* **2010**, *4*, 1259.
- G. A. Ozin, *Adv. Mater.* **2015**, *27*, 1957.
- X. Li, J. Yu, M. Jaroniec, X. Chen, *Chem. Rev.* **2019**, *119*, 3962.
- X. Li, Y. Sun, J. Xu, Y. Shao, J. Wu, X. Xu, Y. Pan, H. Ju, J. Zhu, Y. Xie, *Nat. Energy* **2019**, *4*, 690.
- W. Tu, Y. Zhou, Z. Zou, *Adv. Mater.* **2014**, *26*, 4607.
- S. Das, J. Perez-Ramirez, J. Gong, N. Dewangan, K. Hidajat, B. C. Gates, S. Kawi, *Chem. Soc. Rev.* **2020**, *49*, 2937.
- J. Fu, K. Jiang, X. Qiu, J. Yu, M. Liu, *Mater. Today* **2020**, *32*, 222.
- C. Wang, Z. Xie, K. E. Krafft, W. Lin, *J. Am. Chem. Soc.* **2011**, *133*, 13445.
- Q. Wang, D. Astruc, *Chem. Rev.* **2020**, *120*, 1438.
- A. Kirchon, L. Feng, H. F. Drake, E. A. Joseph, H. C. Zhou, *Chem. Soc. Rev.* **2018**, *47*, 8611.
- A. Dhakshinamoorthy, Z. Li, H. Garcia, *Chem. Soc. Rev.* **2018**, *47*, 8134.
- K. Meyer, M. Ranocchiari, J. A. van Bokhoven, *Energy Environ. Sci.* **2015**, *8*, 1923.
- Y. Chen, D. Wang, X. Deng, Z. Li, *Catal. Sci. Technol.* **2017**, *7*, 4893.
- C. C. Wang, X. D. Du, J. Li, X. X. Guo, P. Wang, J. Zhang, *Appl. Catal., B* **2016**, *193*, 198.
- X. Deng, Z. Li, H. Garcia, *Chem. Eur. J.* **2017**, *23*, 11189.
- X. Yu, L. Wang, S. M. Cohen, *CrystEngComm*, **2017**, *19*, 4126.
- M. Hao, Z. Li, *Sol. RRL* **2020**, 2000454.
- Y. S. Wei, M. Zhang, R. Zou, Q. Xu, *Chem. Rev.* **2020**, DOI: 10.1021/acs.chemrev.9b00766.
- Y. Wang, N. Y. Huang, J. Q. Shen, P. Q. Liao, X. M. Chen, J. P. Zhang, *J. Am. Chem. Soc.* **2018**, *140*, 38.
- Z. Lionet, T.-H. Kim, Y. Horiuchi, S. W. Lee, M. Matsuoka, *J. Phys. Chem. C* **2019**, *123*, 27501.
- M. W. Logan, S. Ayad, J. D. Adamson, T. Dilbeck, K. Hanson, F. J. Uribe-Romo, *J. Mater. Chem. A* **2017**, *5*, 11854.
- C. Li; H. Xu, J. Gao, W. Du, L. Shangguan, X. Zhang, R.-B. Lin, H. Wu, W. Zhou, X. Liu, J. Yao, B. Chen, *J. Mater. Chem. A* **2019**, *7*, 11928.
- Y. Fu, D. Sun, Y. Chen, R. Huang, Z. Ding, X. Fu, Z. Li, *Angew. Chem. Int. Ed.* **2012**, *51*, 3364.
- D. Sun, Y. Fu, W. Liu, L. Ye, D. Wang, L. Yang, X. Fu, Z. Li, *Chem. Eur. J.* **2013**, *19*, 14279.
- D. Wang, R. Huang, W. Liu, D. Sun, Z. Li, *ACS Catal.* **2014**, *4*, 4254.
- E. X. Chen, M. Qiu, Y. F. Zhang, Y. S. Zhu, L. Y. Liu, Y. Y. Sun, X. Bu, J. Zhang, Q. Lin, *Adv. Mater.* **2018**, *30*, 1704388.
- H. Q. Xu, J. Hu, D. Wang, Z. Li, Q. Zhang, Y. Luo, S. H. Yu, H. L. Jiang, *J. Am. Chem. Soc.* **2015**, *137*, 13440.
- X. K. Wang, J. Liu, L. Zhang, L. Z. Dong, S. L. Li, Y. H. Kan, D. S. Li, Y. Q. Lan, *ACS Catal.* **2019**, *9*, 1726.
- X. Y. Dao, J. H. Guo, Y. P. Wei, F. Guo, Y. Liu, W. Y. Sun, *Inorg. Chem.* **2019**, *58*, 8517.
- N. Sadeghi, S. Sharifnia, M. Sheikh Arabi, *J. CO<sub>2</sub> Util.* **2016**, *16*, 450.
- H. Zhang, J. Wei, J. Dong, G. Liu, L. Shi, P. An, G. Zhao, J. Kong, X. Wang, X. Meng, J. Zhang, J. Ye, *Angew. Chem. Int. Ed.* **2016**, *55*, 14310.
- S. L. Xie, J. Liu, L. Z. Dong, S. L. Li, Y. Q. Lan, Z. M. Su, *Chem. Sci.* **2019**, *10*, 185.
- Q. Huang, J. Liu, L. Feng, Q. Wang, W. Guan, L. Z. Dong, L. Zhang, L. K. Yan, Y. Q. Lan, H. C. Zhou, *Natl. Sci. Rev.* **2019**, *7*, 53.

- 34 Z. B. Fang, T. T. Liu, J. Liu, S. Jin, X. P. Wu, X. Q. Gong, K. Wang, Q. Yin, T. F. Liu, R. Cao, H. C. Zhou, *J. Am. Chem. Soc.* **2020**, *142*, 12515.
- 35 P. Horcajada, F. Salles, S. Wuttke, T. Devic, D. Heurtaux, G. Maurin, A. Vimont, M. Daturi, O. David, E. Magnier, N. Stock, Y. Filinchuk, D. Popov, C. Riekkel, G. Férey, C. Serre, *J. Am. Chem. Soc.* **2011**, *133*, 17839.
- 36 P. Horcajada, S. Surble, C. Serre, D. Y. Hong, Y. K. Seo, J. S. Chang, J. M. Greneche, I. Margiolaki, G. Férey, *Chem. Commun.* **2007**, *27*, 2822.
- 37 J. W. Yoon, Y. K. Seo, Y. K. Hwang, J. S. Chang, H. Leclerc, S. Wuttke, P. Bazin, A. Vimont, M. Daturi, E. Bloch, P. L. Llewellyn, C. Serre, P. Horcajada, J. M. Greneche, A. E. Rodrigues, G. Férey, *Angew. Chem. Int. Ed.* **2010**, *49*, 5949.
- 38 S. Bauer, C. Serre, T. Devic, P. Horcajada, M. Jerome, G. Férey, S. Norbert, *Inorg. Chem.* **2008**, *47*, 7568;
- 39 K. M. L. Taylor-Pashow, J. D. Rocca, Z. Xie, S. Tran, W. Lin, *J. Am. Chem. Soc.* **2009**, *131*, 14261.
- 40 D. Feng, K. Wang, Z. Wei, Y. P. Chen, C. M. Simon, R. K. Arvapally, R. L. Martin, M. Bosch, T. F. Liu, S. Fordham, D. Yuan, M. A. Omary, M. Haranczyk, B. Smit,; H. C. Zhou, *Nat. Commun.* **2014**, *5*, 5723.
- 41 H. Dong, X. Zhang, Y. Lu, Y. Yang, Y. P. Zhang, H. L. Tang, F. M. Zhang, Z. D. Yang, X. Sun, Y. Feng, *Appl. Catal., B* **2020**, *276*, 119173.
- 42 L. Z. Dong, L. Zhang, J. Liu, Q. Huang, M. Lu, W. X. Ji, Y. Q. Lan, *Angew. Chem. Int. Ed.* **2020**, *59*, 2659.
- 43 M. Barona, S. Ahn, W. Morris, W. Hoover, J. M. Notestein, O. K. Farha, R. Q. Snurr, *ACS Catal.* **2019**, *10*, 1460.
- 44 J. G. Vitillo, A. Bhan, C. J. Cramer, C. C. Lu, L. Gagliardi, *ACS Catal.* **2019**, *9*, 2870.
- 45 C. Gao, Y. Su, X. Quan, V. K. Sharma, S. Chen, H. Yu, Y. Zhang, J. Niu, *Appl. Catal., B* **2020**, *276*, 119016.
- 46 D. Wang, M. Wang, Z. Li, *ACS Catal.* **2015**, *5*, 6852
- 47 D. Wang, J. Albergo, H. Garcia, Z. Li, *J. Catal.* **2017**, *349*, 156.
- 48 D. Wang, Z. Li, *Res Chem Intermed* **2017**, *43*, 5169.
- 49 G. Kresse, J. Hafner, *Phys Rev B Condens Matter.* **1993**, *47*, 558.
- 50 G. Kresse, J. Furthmuller, *Comput. Mater. Sci.* **1996**, *6*, 15.
- 51 G. Kresse, D. F. Joubert, *Phys. Rev. B* **1999**, *59*, 1758.
- 52 D. Vanderbilt, *Phys Rev B* **1990**, *41*, 7892.
- 53 G. Kresse, J. Hafner, *J. Phys.: Condm. Matter* **1994**, *6*, 8245.
- 54 J. P. Perdew, K. Burke, M. Ernzerhof, *Phys. Rev. Lett.* **1996**, *17*, 3865.
- 55 S. L. Dudarev, G. A. Botton, S. Y. Savrasov, C. J. Humphreys, A. P. Sutton, *Phys. Rev. B* **1998**, *57*, 1505.
- 56 A. A. Peterson, F. Abild-Pedersen, F. Studt, J. Rossmeisl, J. K. Nørskov, *Energy Environ. Sci.* **2010**, *3*, 1311.
- 57 J. K. Nørskov, J. Rossmeisl, A. Logadottir, L. Lindqvist, J. Kitchin, T. Bligaard, H. Jonsson, *J. Phys. Chem. B* **2004**, *108*, 17886.
- 58 S. Guo, H. Zhang, Y. Chen, Z. Liu, B. Yu, Y. Zhao, Z. Yang, B. Han, Z. Liu, *ACS Catal.* **2018**, *8*, 4576.
- 59 K. G. Laurier, F. Vermoortele, R. Ameloot, D. E. De Vos, J. Hofkens, M. B. Roeffaers, *J. Am. Chem. Soc.* **2013**, *135*, 14488.
- 60 C. Hansch, A. Leo, R. W. Taft, *Chem. Rev.* **1991**, *91*, 165.
- 61 W. Ju, A. Bagger, X. Wang, Y. Tsai, F. Luo, T. Möller, H. Wang, J. Rossmeisl, A. S. Varela, P. Strasser, *ACS Energy Lett.* **2019**, *4*, 1663.
- 62 C. Wang, X. M. Liu, M. Zhang, Y. Geng, L. Zhao, Y. G. Li, Z. M. Su, *ACS Sustainable Chem. Eng.* **2019**, *7*, 14102.
- 63 Y. Tian, C. Y. Zhu, L. K. Yan, J. X. Zhao, Z. M. Su, *J. Mater. Chem. A* **2019**, *7*, 15341.
- 64 Etienne Boutin, Min Wang, John C. Lin, Matthieu Mesnage, Daniela Mendoza, B. Lassalle-Kaiser, C. Hahn, T. F. Jaramillo, M. Robert, *Angew. Chem. Int. Ed.* **2019**, *58*, 16172.

View Article Online  
DOI: 10.1039/D0TA10278D